



DOI: 10.29026/oea.2020.190017

Controlling plasmon-exciton interactions through photothermal reshaping

Aiqin Hu^{1,2}, Shuai Liu^{1,3}, Jingyi Zhao¹, Te Wen¹, Weidong Zhang¹,
Qihuang Gong^{1,2}, Yongqiang Meng³, Yu Ye¹ and Guowei Lu^{1,2*}

We investigated the plasmon-exciton interactions in an individual gold nanorod (GNR) with monolayer MoS₂ at room temperature with the single-particle spectroscopy technique. To control the plasmon-exciton interaction, we tuned the local surface plasmon resonance of an individual GNR *in-situ* by employing the photothermal reshaping effect. The scattering spectra of the GNR-MoS₂ hybrids exhibited two dips at the frequencies of the A and B excitons of monolayer MoS₂, which were caused by the plasmon-induced resonance energy transfer effect. The resonance energy transfer rate increased when the surface plasmon resonance of the nanorod matched well with the exciton transition energy. Also, we demonstrated that the plasmon-enhanced fluorescence process dominated the photoluminescence of the GNR-MoS₂ hybrid. These results provide a flexible way to control the plasmon-exciton interaction in an all-solid-state operating system at room temperature.

Keywords: gold nanorod; MoS₂; hybrid; scattering; photoluminescence; single nanoparticle

Hu A Q, Liu S, Zhao J Y, Wen T, Zhang W D et al. Controlling plasmon-exciton interactions through photothermal reshaping. *Opto-Electron Adv* 3, 190017 (2020).

Introduction

Plasmon-exciton hybrids, as platforms for investigating light-matter interactions with various mechanisms such as plasmon-induced resonance energy transfer (RET)^{1,2}, Fano interference³⁻⁵, strong coupling⁶⁻¹², and plasmon-enhanced absorption and emission¹³⁻²³ have attracted much attention. Monolayer transition metal dichalcogenides (TMDCs) have evoked strong interests owing to their fascinating optical properties and flexible features for integration²⁴. However, the atomic thickness causes weak optical absorption (<11%) of excitons in monolayer TMDCs, which thereby limits their optoelectronic applications. Fortunately, the metal nanoparticles can facilitate light-matter interactions owing to the surface plasmon resonance, contributing to the enhanced absorption of visible light^{25,26}. The surface plasmon can

concentrate light beyond the diffraction limit²⁷, and that is why metal nanoparticles have been exploited to enhance light-matter interactions in 2D materials. Besides, the large exciton binding energy of TMDCs yields a substantial oscillator strength, which boosts the interactions of plasmon-exciton in the hybrids consisting of plasmonic nanostructures and monolayer TMDCs^{6,11,28}.

Recently, many composite structures exhibited strong plasmon-exciton coherent interactions at the single plasmonic nanostructure level at room temperature, such as WS₂ and Au nanorods¹⁰, WSe₂ and Ag nanorods⁷, WSe₂ and nanoparticle-on-mirror structures¹², mono- and multi-layer WSe₂ and gold bipyramids²⁹, and WSe₂ and nanocube-over-mirror systems³⁰. In addition to the neutral exciton resonances, TMDCs also support charged exciton resonances^{31,32}. Thus, the interaction between charged exciton in monolayer WS₂ and a silver nanoprism

¹State Key Laboratory for Mesoscopic Physics, Collaborative Innovation Center of Quantum Matter, Nano-optoelectronics Frontier Center of the Ministry of Education, School of Physics, Peking University, Beijing 100871, China. ²Collaborative Innovation Center of Extreme Optics, Shanxi University, Taiyuan, Shanxi 030006, China. ³School of Materials Science and Engineering, Hebei University of Science and Technology, Shijiazhuang 050018, China.

*Correspondence: G W Lu, E-mail: guowei.lu@pku.edu.cn

Received: 15 May 2019; Accepted: 17 June 2019; Published: 20 January 2020

has been achieved at cryogenic temperatures⁸. The coupling strength is proportional to the exciton transition dipole moment μ and the single photon electric field E of the cavity³³. Hence, highly confined exciton in the in-plane direction of the monolayer TMDCs couples efficiently with plasmonic nanostructures on the surface. Also, the behavior of the plasmon-exciton interaction is dependent on the detuning between the plasmon resonances and exciton energy. The detuning can be tailored by changing the exciton energy with various ambient temperature¹⁰ or the number of layers of the TMDCs²⁹, but tuning the exciton energy doesn't work efficiently at room temperature. Besides, control of plasmon-exciton coupling can be achieved by tailoring the local surface plasmon resonances (LSPRs) of the metal nanostructures. Previous studies have demonstrated for adjusting the plasmon resonance energy through successive deposition of a dielectric layer onto a nanoparticle^{7,30}, using different aspect ratios of the gold nanorods¹⁰, or changing the environmental dielectric refractive index³. Nevertheless, an alternative and efficient way to tune the plasmon resonant energy remains to be explored.

In this study, we demonstrate that the photothermal reshaping method^{34–37} can be applied to tune the LSPRs of metallic nanoparticles *in-situ*. The hybrid consisting of gold nanorod (GNR) and monolayer MoS₂ was assembled by employing the atomic force microscopy (AFM) nanomanipulation technique³⁸. We investigated the scat-

tering and photoluminescence (PL) spectra of the hybrid system at the single-particle level. The plasmon-exciton interactions were discussed and analyzed with the aid of numerical simulations and the semi-classical coupled oscillator model. The spectra of the GNR-MoS₂ hybrid can be explained as plasmon-induced resonance energy transfer. The plasmon-exciton interactions could be tuned precisely and efficiently *in-situ* with the photothermal reshaping method.

Results and discussion

Figure 1(a) shows the schematic diagram of the GNR-MoS₂ hybrid system. The GNRs were synthesized through a seed-mediated wet chemical method³⁹. First, to obtain an average spacing of several micrometers for the single-particle-level measurements, a dilute aqueous solution of the GNRs was spin-casted onto a glass coverslip. Figure 1(b) shows the normalized extinction spectra of the GNRs in aqueous solution, and the inset shows a representative transmission electron microscopy imaging with a scale bar of 100 nm. Second, we transferred the monolayer MoS₂ onto the glass coverslip. The MoS₂ was obtained by a chemical vapor deposition method. Then, the sample was investigated by the single-particle spectroscopy^{40,41}. Briefly, the microspectroscopy system integrated white-light dark-field scattering, photoluminescence, and AFM. The continuous-wave laser at a wavelength of 532 nm was employed as the illumination

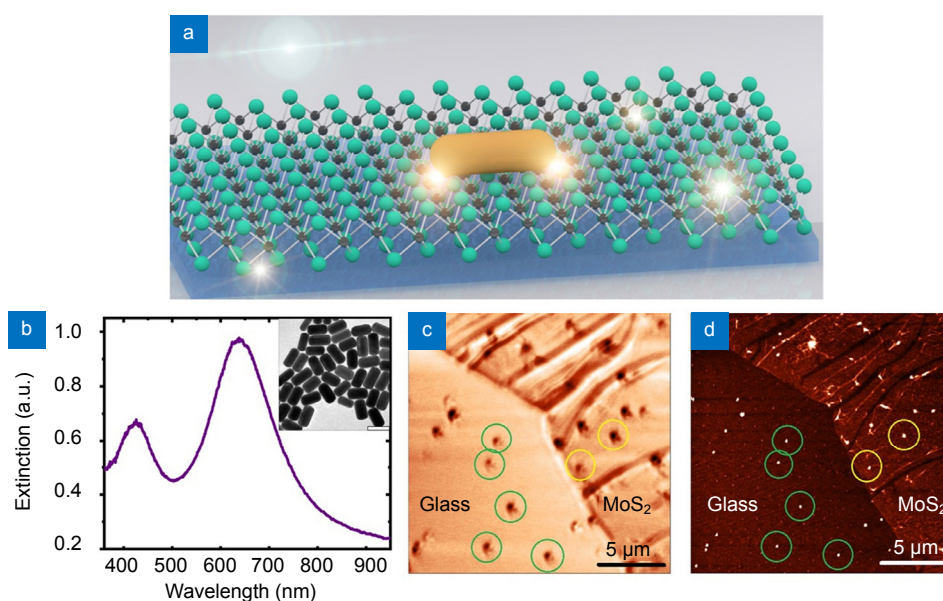


Fig. 1 | (a) Schematic diagram of GNRs-MoS₂ hybrid on the glass substrate. (b) Extinction spectra of GNRs in aqueous solution. Inset: transmission electron micrographs of the GNRs with a scale bar of 100 nm. (c), (d) Optical confocal scanning image and AFM image of the GNRs-MoS₂, respectively. The green and yellow circles indicate the positions of single GNR on glass and MoS₂ monolayer, respectively, with a scale bar of 5 μm.

source. An oil-immersion objective lens with a numerical aperture of 1.3 was used for both excitation and collection, and the diameter of the laser focus spot size was about ~ 500 nm. In the experiment, the optical confocal scanning images and AFM images were used to confirm the presence of the GNRs. Figures 1(c) and 1(d) show the optical and AFM images of the same area of the GNRs-MoS₂ hybrid, respectively. The green circles indicate the locations of individual GNRs on the glass and the yellow circles indicate the individual GNRs on MoS₂ flakes. The optical setup based on the NTEGRA platform (NT-MDT, NTEGRA Spectra, Russia) has been described in detail previously^{42,43}. The scattering and PL spectra of the same GNRs can be measured *in-situ*. The GNRs were chosen as plasmonic nanocavities because their longitudinal surface plasmon resonances (LSP) mode can be tailored elaborately by photothermal reshaping.

At first, we tuned *in-situ* the LSPR peak of a single GNR on a bare glass substrate by using the photothermal reshaping effect (Fig. 2(a))⁴⁴. The laser-induced shape transformation made the contour of the nanoparticle change from rod shape to spherical shape or circle disk shape. In our experiments, the laser power could be tuned from 50 μ W to 10 mW to heat the GNRs (once for 5 seconds) gradually. We noted that the maximum laser

power we used in the present experiment was ~ 4.2 mW. For example, we selected a GNR with an original LSPR at a wavelength of 685 nm on the glass. We measured the scattering spectra (Fig. 2(a)) of the GNR after each reshaping step. As can be seen from Fig. 2(b), the scattering spectra gradually blue-shifted, the scattering intensity simultaneously decreased, and the full width at half maximum (FWHM) of scattering increased about 30 meV after the photothermal reshaping. We noted that different GNRs exhibited different reshaping progress under the same laser heating power, so the exact reshaping process remained to be determined. To understand the photothermal reshaping process fully, we used the finite-difference time-domain (FDTD) method to simulate the scattering, as shown in Fig. S1. To simulate the reshaping approximately, we changed the length-diameter ratio (L/D) of an ellipsoid (30 nm \times 30 nm \times 90 nm) without changing its volume and height. When the nanoparticle reshaped from a rod to a circle disk, the scattering spectra were blue-shifted (Fig. S1(a)), the scattering intensity decreased (red line) while the FWHM changed slightly (black line) (Fig. S1(b)). The calculated and measured scattering spectra agreed very well. Then, we tested the influence of laser heating on pristine MoS₂ monolayer on a glass substrate. We heated the MoS₂ flake

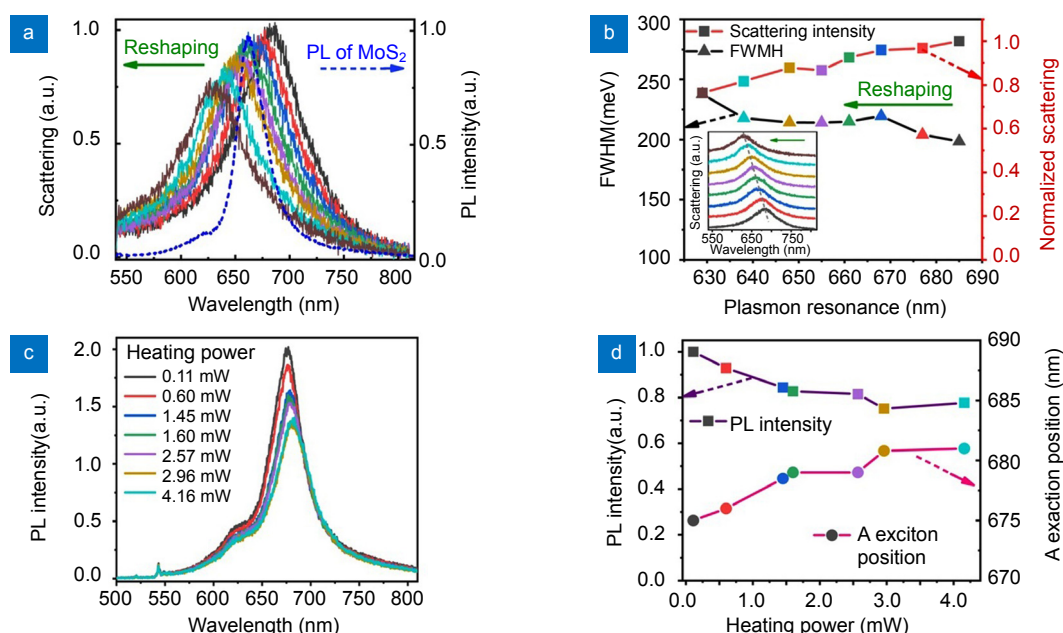


Fig. 2 | Photothermal reshaping of a single GNR on the glass substrate. (a) Scattering spectra of a GNR on the glass tuned by photothermal reshaping effect through controlling the illumination power. The blue-dashed line in (a) is the photoluminescence spectra of the MoS₂ monolayer. (b) FWHM and intensity of scattering spectra during the photothermal reshaping. Inset shows the blue-shift of the plasmon resonance of GNR. The color in (b) corresponds to the color of the scattering spectra in (a). (c) Influence of laser power (~ 0.11 mW to ~ 4.16 mW) on monolayer MoS₂ on the glass. (d) PL intensity and A exciton position changes during the photothermal reshaping. Excitation laser wavelength: 532 nm. Excitation power: 110 μ W. Integration time: 0.5 s.

approximately 10 s, using the same 532 nm laser, and varied the laser's power from 110 μ W to 4.2 mW. After each heating step, we measured the PL spectra using an excitation power of 110 μ W. As shown in Fig. 2(c), the PL intensity decreased by about 25%, but the spectral shape exhibited no changes when the heating power was lower than 4.2 mW (as shown in Fig. 2(c) and Fig. S2(a)). Meanwhile, the peak of the A exciton red shifted approximately 5 nm after the heating. We repeated this experiment over 5 times. The results indicated that laser heating power up to 4.2 mW had no damage on the monolayer MoS₂. However, when the power was increased up to 6 mW, the PL spectral shape was deformed, which implied that the monolayer MoS₂ was damaged (Fig. S2(b)). In brief, we demonstrated that the LSPR of GNRs could be tuned by the photothermal reshaping method, and the monolayer MoS₂ was stable under a laser heating power of \sim 4 mW^{44,45}. Hence, the photothermal reshaping effect is a convenient and efficient way to tune the detuning between the plasmon of GNR and the exciton of monolayer MoS₂.

To investigate the plasmon-exciton interaction, the GNR-MoS₂ hybrids were assembled by using the AFM

nanomanipulation technique⁴⁶. We moved the GNRs from the glass surface onto the monolayer MoS₂ flake. Figure 3 shows the representative scattering and PL spectra of the same GNR before and after coupling with the monolayer MoS₂ flake. As shown in Fig. 3(a), a typical GNR on the glass substrate exhibited an LSPR peak at 685 nm, and the FWHM of the scattering spectra was 206 meV ($\gamma_{\text{pl}} = 206$ meV). The broad FWHM arose from the large size of the GNR (average size of approximately 50 nm \times 120 nm). It should be noted that the LSPR peak of the GNRs red shifted when the GNRs were moved from the glass to the MoS₂ owing to the increase of the surrounding medium index. The pristine monolayer MoS₂ exhibited an exciton emission centering at 673 nm, with an FWHM of 79 meV ($\gamma_{\text{ex}} = 79$ meV) (Fig. 3(b) and Fig. S3(a)). Raman spectra, as shown in Fig. 3(b) inset, displayed two peaks at approximately 408 cm⁻¹ and 388 cm⁻¹ that matched the out-of-plane A_{1g} mode and the in-plane E_{2g}¹ mode of monolayer MoS₂, respectively. Raman spectra, an accurate identifying⁴⁷, confirmed the presence of monolayer MoS₂. Figures 3(b) and S3(a) show the PL spectra of monolayer MoS₂ on the glass. A Lorentz-shaped line fitted the two peaks at wavelengths of

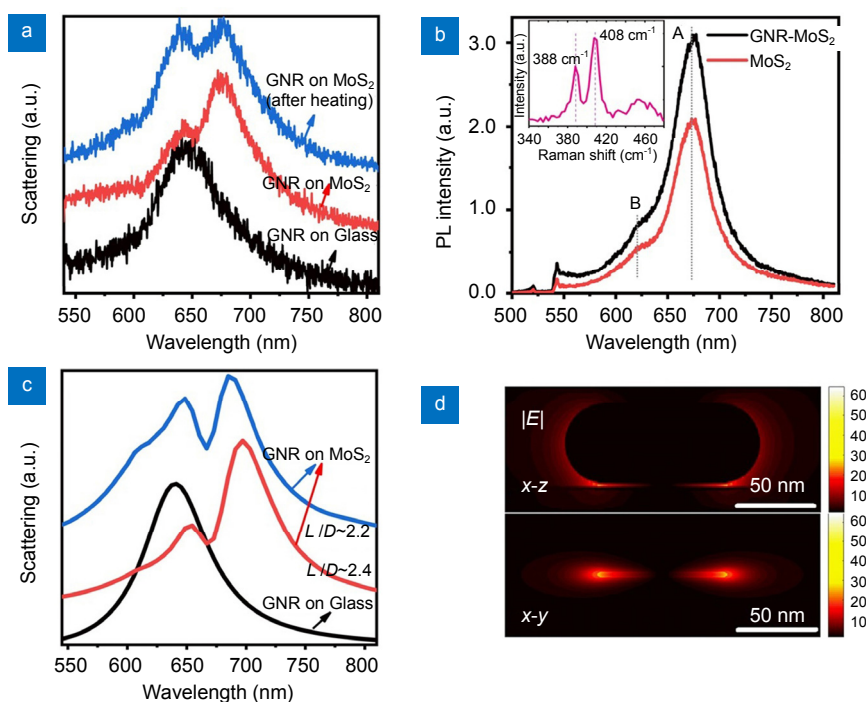


Fig. 3 | (a) Normalized scattering spectra of a GNR on glass (black), the same GNR moved onto MoS₂ (red), and the GNR on MoS₂ after heating (blue). (b) Photoluminescence spectra of MoS₂ monolayer without (red) and with (black) GNR. The black dashed line in (b) marks the A (right) and B (left) excitons absorption peak. Inset: Raman spectra of MoS₂ monolayer with the A_{1g} peak (408 cm⁻¹) and E_{2g}¹ peak (388 cm⁻¹). Excitation laser wavelength: 532 nm. Excitation power: 110 μ W. Integration time: 0.5 s. (c) Calculated scattering spectra using the FDTD method corresponding to the experimental spectra shown in (a). Scattering spectra of a GNR ($L/D \sim 2.4$) on glass (black), the same GNR ($L/D \sim 2.4$) on MoS₂ (red) and another GNR ($L/D \sim 2.2$) on MoS₂ (blue). (d) Near-field distributions: the calculated near-field distribution $|E|$ in the x - z plane ($y=0$ nm) (upper) and in the x - y plane ($z=0$ nm) (lower), i.e., the interface between GNR and MoS₂.

673 nm and 620 nm, respectively, which matched well with the energy of the A exciton and B exciton of monolayer MoS₂. The energy difference between A and B exciton transition is due to the large spin-orbit splitting in the valence band⁴⁸. After moving the GNR onto the monolayer MoS₂ flake, the PL intensity of the MoS₂-GNR hybrid increased ~1.4-folds, and the PL spectral peak was red-shifted approximately 3 nm, as shown in Figs. 3(b) and S3(b). The GNR can enhance the excitation and emission process as an optical antenna⁴⁹. The high refractive index ($n \sim 3$) of the MoS₂ layers resulted in the red-shift of LSPR peak, and the plasmonic antenna effect modified the emission spectral shape⁵⁰. Additionally, the enhancement around 540 nm of the PL spectrum mostly attributed to the intrinsic metal luminescence from the GNR⁵⁰.

Regarding the scattering spectra of the GNR-MoS₂ hybrid shown in Fig. 3(a) (red line), a dip was observed at 661 nm and illustrated more than a 30% decrease of the maximum intensity. The LSPR of GNR was on the low-energy side compared with the exciton energy. To change the LSPR of the GNR, we heated the hybrid using a 532-nm laser with a power of 1.4 mW for 5 seconds. The scattering spectra were shown in Fig. 3(a) (blue line). Scattering dips showed a decrease in the maximum intensity of more than 19%. When the LSPR was excited, the local electromagnetic density of GNR-MoS₂ hybrids increased, and the absorption of the hybrid enhanced⁵¹. It was necessary to heat the GNR to increase the plasmon-exciton interaction owing to the relative small dipole moment of the exciton of MoS₂. The photothermal reshaping could volatilize the impurities, which led to a larger contact area or shorter separation between the GNR and the MoS₂ and then enhances the interaction⁴⁴. These results demonstrated that it was feasible to modify the plasmon-exciton interaction through the photothermal effect. To further understand the plasmon-exciton interaction of GNR-MoS₂ hybrids, we calculated the scattering spectra and near-field electromagnetic field distributions by employing the FDTD method (Figs. 3(c) and 3(d)). The normalized scattering spectra (shown in Fig. 3(c)) of the GNR-MoS₂ hybrid exhibited two distinct dips around the A and B excitons of MoS₂, in accord with the experimental results shown in Fig. 3(a). The exciton transition energies varied between different MoS₂ flakes owing to the presence of impurities, defects, and tensions from the substrate. A similar shift between the experimental and simulation results has also been

reported previously¹⁰. Moreover, as shown in Fig. 3(d), the plasmonic near field was strongly confined to the interface between the MoS₂ surface and GNR (upper panel). The localized electromagnetic field greatly enhanced at the GNR-MoS₂ interface. Moreover, the strongest enhancements located near the two ends of the GNR. Such a highly confined enhanced field should mainly contribute to the strong plasmon-exciton interaction.

To demonstrate the convenience and flexibility of the photothermal reshaping method, we stepwise heated *in-situ* the GNR-MoS₂ hybrid. After each 5 s heating step, we measured the scattering spectra of the same GNR-MoS₂ hybrid. As shown in Fig. 4(a), the scattering spectra changed with the laser heating power from 0.11 mW to 1.93 mW. The LSPR of the GNR was blue-shifted as the laser power increased gradually. At first, the LSPR of GNR was on the low-energy side of the exciton transition, so the low-energy branch dominated the scattering intensity. As the LSPR blue-shifted and the detuning decreased, the low-energy branch intensity reduced gradually. When the LSPR of GNR overlapped with the exciton energy, that is, plasmon-exciton detuning was zero, the strengths of the low- and high-energy branches were comparable with each other. Furthermore, the LSPR of GNR was on the high-energy side of the exciton, so the high-energy branch dominated the scattering intensity (Fig. S4). Figure 4(a) shows the dips in the scattering spectra, which corresponded to the peaks of the A exciton of monolayer MoS₂ (vertical purple dashed line). We noted that the dips of scattering spectra showed a decrease in the maximum intensity of more than 19%. These deep dips implied that the scattering spectra of the GNR-MoS₂ hybrids did not arise from a pure superposition of the optical absorption (less than 11%) of monolayer MoS₂ and the scattering spectra of an individual GNR. The interactions of the GNR and MoS₂ monolayer were explained as a plasmon-induced RET process. The monolayer MoS₂ and GNRs exchanged energy coherently until the exciton of MoS₂ or the plasmon of GNRs was wholly decayed. Besides, we tested the GNR-WS₂ hybrid using the same experimental method. As shown in Fig. S5, a scattering spectral dip also occurred at ~610 nm owing to the A exciton of the WS₂ monolayer.

As shown in Fig. S4(a), after fitting the scattering spectra with two-Lorentz line shapes, the intensities of the upper-energy branch (UEB) and lower-energy branch (LEB) changed with the heating power. As can be seen

from Fig. S3(b), the UEB intensity increased while the LEB intensity decreased gradually. However, the linewidth of UEB increased obviously, but the linewidth of LEB almost did not change (Fig. 4(c)). According to Fig. 4(c) and Fig. 2(b), we concluded that the increases of the UEB linewidth mainly arose from the shape changes of the GNR during the photothermal reshaping. The different detuning between the plasmon and exciton (Fig. 4(d)) resulted in anti-crossing plexciton dispersion, which could be fitted to the semi-classical coupled oscillator model^{33,52}, as given in equation S1 (Supplementary Information). However, it was not fitted well. Although the peak of the UEB was blue-shifted, the peak of LEB exhibited a small shift. Thus, we excluded the possibility of strong coupling because it did not rigorously satisfy the criterion ($2\Omega_R > \gamma_{ex} + \gamma_{pl}$) for strong coupling. Hence, the present plasmon-exciton interactions of the GNR-MoS₂ hybrid cannot be understood as strong coupling. Furthermore, we also measured the scattering spectra of the GNR-WS₂ hybrid (Fig. S5). After heating, a mode splitting up to 163 meV could be obtained from the scattering

spectra, which resulted from the relatively large exciton transition dipole moments of WS₂. So the result of GNR-WS₂ satisfied the criterion ($2\Omega_R > \gamma_{ex} + \gamma_{pl}$) for strong coupling, which resulted from the relatively large exciton transition dipole moments of WS₂.

Furthermore, the plasmon-enhanced fluorescence of the GNR-MoS₂ hybrid was investigated and analyzed. The PL intensity of the pristine MoS₂ was almost independent of the excitation polarization, as shown in Fig. S6(d). But the polarization dependence of the hybrid was similar to the polarization behavior of the individual GNR. Here, the enhanced PL was defined as the difference between the PL spectra obtained with two orthogonal excitation polarization (Fig. S7), that is, the difference between the maximum and minimum spectra. The plasmon-enhanced PL spectra under different laser heating powers were shown in Fig. 4(b). Before heating, the enhanced PL spectra only exhibited one peak at the position of the A exciton (Fig. 4(b1)) and kept the spectral shape the same as that of the pristine MoS₂. It meant that the plasmon-exciton interactions were weak. After heating

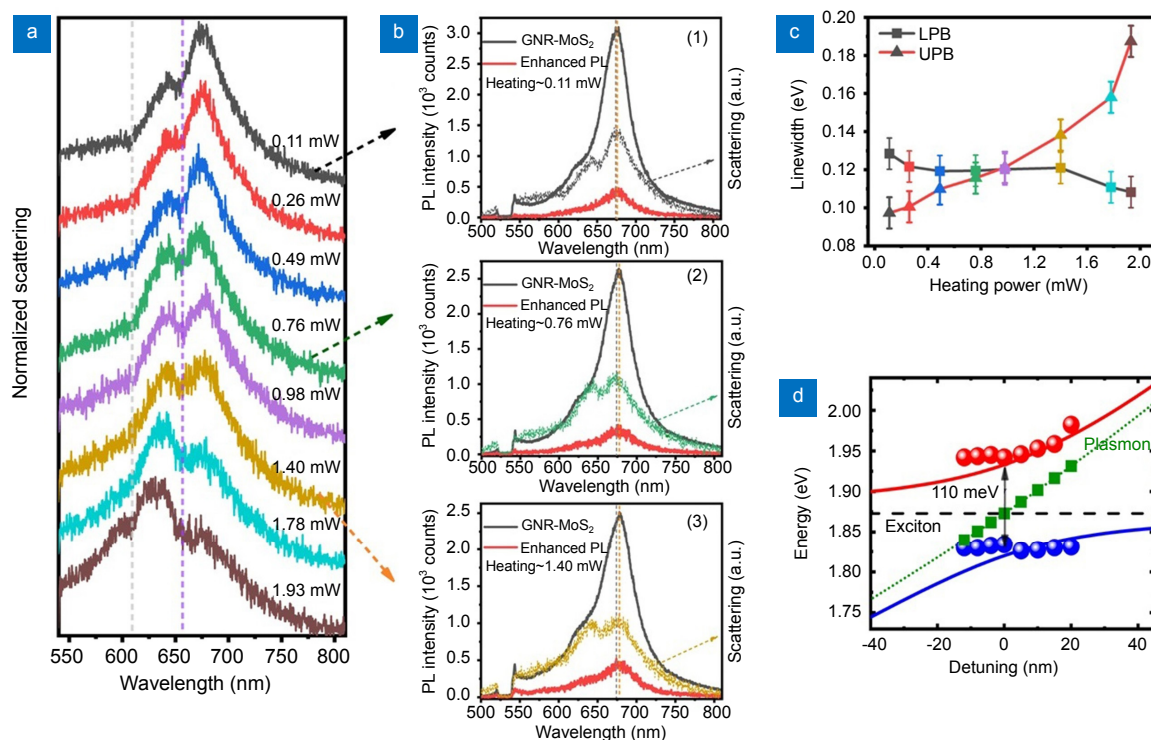


Fig. 4 | Plasmon exciton interaction in the GNR-MoS₂ hybrid. (a) Scattering spectra of individual GNR coupled to the monolayer MoS₂ flake. The vertical purple and grey dashed lines in (a) mark the A and B excitons absorption peaks. (b) Corresponding PL spectra (black line) of GNR-MoS₂ hybrid during the photothermal reshaping. The vertical orange dashed line in (b) marks A exciton absorption peak of MoS₂ with GNR, and the vertical gray dashed line in (b) marks A exciton absorption peak of pristine MoS₂ without GNR. The dashed curve in (b) shows the scattering spectra. (c) Changes in the linewidth of scattering spectra of GNR-MoS₂ hybrid with heating power. The color in (c) corresponds to the color of the scattering spectra in (a). (d) Hybrid plasmon-exciton branches as a function of detuning. The dots (red spheres correspond to upper energy branch, blue sphere to lower energy branch, green squares to plasmon resonance) correspond to extracted experimental values, and the curves are theoretical results. Black and green lines indicate the dispersion of the uncoupled exciton and plasmon, respectively.

with a power of 0.76 mW and 1.40 mW (Fig. S7(e) and Fig. S7(f)), respectively, the spectral shape of the enhanced PL was not consistent with that of the pristine MoS₂. Another spectral shoulder appeared at a shorter wavelength. Considering the blue-shift of the LSPR of an individual GNR, we proposed that this new shoulder of the PL spectra arose from the plasmon emission of the GNR. The shoulder could be the direct luminescence from the GNR or the plasmon-modified fluorescence of the MoS₂. Although a scattering spectral splitting of the GNR-MoS₂ was noticeable, the PL spectral shape did not split. Hence, the plasmon-enhanced fluorescence process should dominate the PL spectral shape of the GNR-MoS₂ hybrid, and the plasmon-exciton interaction belongs to the weak coupling range.

Conclusions

In summary, we employed the AFM nanomanipulation technique and single-particle spectroscopy to investigate the GNR-MoS₂ hybrid at room temperature. Based on the photothermal reshaping effect, we successfully tuned *in-situ* LSPR of an individual GNR and then controlled the plasmon-exciton interactions. The scattering spectral shape of the GNR-MoS₂ was explained as the plasmon-induced RET. Moreover, the rate of RET increased when the LSPR of GNR matched well with the exciton energy of MoS₂. Also, the PL emission of the GNR-MoS₂ hybrid was dominated by the plasmon-enhanced fluorescence process. We demonstrated that the photothermal reshaping method was efficient to tailoring the LSPR of the metal nanoparticles at the single-particle level. This research provides a new route to control the plasmon-exciton interaction.

References

1. Wang M S, Li W, Scarabelli L, Rajeeva B B, Terrones M et al. Plasmon-trion and plasmon-exciton resonance energy transfer from a single plasmonic nanoparticle to monolayer MoS₂. *Nanoscale* **9**, 13947–13955 (2017).
2. Li J T, Cushing S K, Meng F K, Senty T R, Bristow A D et al. Plasmon-induced resonance energy transfer for solar energy conversion. *Nat Photonics* **9**, 601–607 (2015).
3. Wang M S, Krasnok A, Zhang T Y, Scarabelli L, Liu H et al. Tunable fano resonance and plasmon-exciton coupling in single Au nanotriangles on monolayer WS₂ at room temperature. *Adv Mater* **30**, 1705779 (2018).
4. Zhang W, Govorov A O, Bryant G W. Semiconductor-metal nanoparticle molecules: hybrid excitons and the nonlinear fano effect. *Phys Rev Lett* **97**, 146804 (2006).
5. Lee B, Park J, Han G H, Ee H S, Naylor C H et al. Fano resonance and spectrally modified photoluminescence enhancement in monolayer MoS₂ integrated with plasmonic nanoantenna array. *Nano Lett* **15**, 3646–3653 (2015).
6. Liu X Z, Galfsky T, Sun Z, Xia F N, Lin E C et al. Strong light-matter coupling in two-dimensional atomic crystals. *Nat Photonics* **9**, 30–34 (2015).
7. Zheng D, Zhang S P, Deng Q, Kang M, Nordlander P et al. Manipulating coherent plasmon-exciton interaction in a single silver nanorod on monolayer WSe₂. *Nano Lett* **17**, 3809–3814 (2017).
8. Cuadra J, Baranov D G, Wersäll M, Verre R, Antosiewicz T J et al. Observation of tunable charged exciton polaritons in hybrid monolayer WS₂-plasmonic nanoantenna system. *Nano Lett* **18**, 1777–1785 (2018).
9. Wersäll M, Cuadra J, Antosiewicz T J, Balci S, Shegai T. Observation of mode splitting in photoluminescence of individual plasmonic nanoparticles strongly coupled to molecular excitons. *Nano Lett* **17**, 551–558 (2017).
10. Wen J X, Wang H, Wang W L, Deng Z X, Zhuang C et al. Room-temperature strong light-matter interaction with active control in single plasmonic nanorod coupled with two-dimensional atomic crystals. *Nano Lett* **17**, 4689–4697 (2017).
11. Liu W J, Lee B, Naylor C H, Ee H S, Park J et al. Strong exciton-plasmon coupling in MoS₂ coupled with plasmonic lattice. *Nano Lett* **16**, 1262–1269 (2016).
12. Kleemann M E, Chikkaraddy R, Alexeev E M, Kos D, Carnegie C et al. Strong-coupling of WSe₂ in ultra-compact plasmonic nanocavities at room temperature. *Nat Commun* **8**, 1296 (2017).
13. Gao W, Lee Y H, Jiang R B, Wang J F, Liu T X et al. Localized and continuous tuning of monolayer MoS₂ photoluminescence using a single shape-controlled Ag nanoantenna. *Adv Mater* **28**, 701–706 (2016).
14. Akselrod G M, Ming T, Argyropoulos C, Hoang T B, Lin Y X et al. Leveraging nanocavity harmonics for control of optical processes in 2D semiconductors. *Nano Lett* **15**, 3578–3584 (2015).
15. Najmaei S, Mlayah A, Arbouet A, Girard C, Léotin J et al. Plasmonic pumping of excitonic photoluminescence in hybrid MoS₂-Au nanostructures. *ACS Nano* **8**, 12682–12689 (2014).
16. Lee K C J, Chen Y H, Lin H Y, Cheng C C, Chen P Y et al. Plasmonic gold nanorods coverage influence on enhancement of the photoluminescence of two-dimensional MoS₂ monolayer. *Sci Rep* **5**, 16374 (2015).
17. Liu J T, Tong H, Wu Z H, Huang J B, Zhou Y S. Greatly enhanced light emission of MoS₂ using photonic crystal heterojunction. *Sci Rep* **7**, 16391 (2017).
18. Wang Z, Dong Z G, Gu Y H, Chang Y H, Zhang L et al. Giant photoluminescence enhancement in tungsten-diselenide-gold plasmonic hybrid structures. *Nat Commun* **7**, 11283 (2016).
19. Johnson A D, Cheng F, Tsai Y, Shih C K. Giant enhancement of defect-bound exciton luminescence and suppression of band-edge luminescence in monolayer WSe₂-Ag plasmonic hybrid structures. *Nano Lett* **17**, 4317–4322 (2017).
20. Wang Q X, Guo J, Ding Z J, Qi D Y, Jiang J Z et al. Fabry-perot cavity-enhanced optical absorption in ultrasensitive tunable photodiodes based on hybrid 2D materials. *Nano Lett* **17**, 7593–7598 (2017).
21. Sobhani A, Lauchner A, Najmaei S, Ayala-Orozco C, Wen F F et al. Enhancing the photocurrent and photoluminescence of single crystal monolayer MoS₂ with resonant plasmonic nanoshells. *Appl Phys Lett* **104**, 031112 (2014).
22. Palacios E, Park S, Butun S, Lauhon L, Aydin K. Enhanced

- radiative emission from monolayer MoS₂ films using a single plasmonic dimer nanoantenna. *Appl Phys Lett* **111**, 031101 (2017).
23. Butun S, Tongay S, Aydin K. Enhanced light emission from large-area monolayer MoS₂ using plasmonic nanodisc arrays. *Nano Lett* **15**, 2700–2704 (2015).
 24. Mak K F, Lee C, Hone J, Shan J, Heinz T F. Atomically thin MoS₂: a new direct-gap semiconductor. *Phys Rev Lett* **105**, 136805 (2010).
 25. Xu K C, Wu J G, Tan C F, Ho G W, Wei A et al. Ag-CuO-ZnO metal-semiconductor multiconcentric nanotubes for achieving superior and perdurable photodegradation. *Nanoscale* **9**, 11574–11583 (2017).
 26. Rahmani M, Leo G, Brenner I, Zayats A V, Maier S A et al. Non-linear frequency conversion in optical nanoantennas and metasurfaces: materials evolution and fabrication. *Opto-Electron Adv* **1**, 180021 (2018).
 27. Upputuri P K, Pramanik M. Microsphere-aided optical microscopy and its applications for super-resolution imaging. *Opt Commun* **404**, 32–41 (2017).
 28. Zhang L, Gogna R, Burg W, Tutuc E, Deng H. Photonic-crystal exciton-polaritons in monolayer semiconductors. *Nat Commun* **9**, 713 (2018).
 29. St ü hrenberg M, Munkhbat B, Baranov D G, Cuadra J, Yankovich A B et al. Strong light-matter coupling between plasmons in individual gold Bi-pyramids and excitons in mono- and multilayer WSe₂. *Nano Lett* **18**, 5938–5945 (2018).
 30. Sun J W, Hu H T, Zheng D, Zhang D X, Deng Q et al. Light-emitting plexciton: exploiting plasmon-exciton interaction in the intermediate coupling regime. *ACS Nano* **12**, 10393–10402 (2018).
 31. Ross J S, Klement P, Jones A M, Ghimire N J, Yan J Q et al. Electrically tunable excitonic light-emitting diodes based on monolayer WSe₂ p-n junctions. *Nat Nanotechnol* **9**, 268–272 (2014).
 32. Mak K F, He K L, Lee C, Lee G H, Hone J et al. Tightly bound trions in monolayer MoS₂. *Nat Mater* **12**, 207–211 (2013).
 33. Chikkaraddy R, De Nijs B, Benz F, Barrow S J, Scherman O A et al. Single-molecule strong coupling at room temperature in plasmonic nanocavities. *Nature* **535**, 127–130 (2016).
 34. Yorulmaz M, Khatua S, Zijlstra P, Gaiduk A, Orrit M. Luminescence quantum yield of single gold nanorods. *Nano Lett* **12**, 4385–4391 (2012).
 35. He Y B, Lu G W, Shen H M, Cheng Y Q, Gong Q H. Strongly enhanced raman scattering of graphene by a single gold nanorod. *Appl Phys Lett* **107**, 053104 (2015).
 36. Della Picca F, Gutiérrez M V, Bragas A V, Scarpellini A F. Monitoring the photothermal reshaping of individual plasmonic nanorods with coherent mechanical oscillations. *J Phys Chem C* **122**, 29598–29606 (2018).
 37. Wang J, Chen Y C, Chen X, Hao J M, Yan M et al. Photothermal reshaping of gold nanoparticles in a plasmonic absorber. *Opt Express* **19**, 14726–14734 (2011).
 38. Shafiei F, Monticone F, Le K Q, Liu X X, Hartsfield T et al. A subwavelength plasmonic metamolecule exhibiting magnetic-based optical Fano resonance. *Nat Nanotechnol* **8**, 95–99 (2013).
 39. Lu G W, Hou L, Zhang T Y, Liu J, Shen H M et al. Plasmonic sensing via photoluminescence of individual gold nanorod. *J Phys Chem C* **116**, 25509–25516 (2012).
 40. Shen H M, Chou R Y, Hui Y Y, He Y B, Cheng Y Q et al. Directional fluorescence emission from a compact plasmonic-diamond hybrid nanostructure. *Laser Photonics Rev* **10**, 647–655 (2016).
 41. Cao Z M, He Y B, Cheng Y Q, Zhao J Y, Li G T et al. Nano-gap between a gold tip and nanorod for polarization dependent surface enhanced Raman scattering. *Appl Phys Lett* **109**, 233103 (2016).
 42. Zhang T Y, Shen H M, Lu G W, Liu J, He Y B et al. Single bipyramid plasmonic antenna orientation determined by direct photoluminescence pattern imaging. *Adv Opt Mater* **1**, 335–342 (2013).
 43. Lu G W, Wang Y W, Chou R Y, Shen H M, He Y B et al. Directional side scattering of light by a single plasmonic trimer. *Laser Photonics Rev* **9**, 530–537 (2015).
 44. He Y B, Lu G W, Shen H M, Cheng Y Q, Gong Q H. Strongly enhanced Raman scattering of graphene by a single gold nanorod. *Appl Phys Lett* **107**, 053104 (2015).
 45. He Y B, Xia K Y, Lu G W, Shen H M, Cheng Y Q et al. Surface enhanced anti-Stokes one-photon luminescence from single gold nanorods. *Nanoscale* **7**, 577–582 (2015).
 46. Zhao J Y, Cao Z M, Cheng Y Q, Xu J N, Wen T et al. In situ optical study of gold nanorod coupling with graphene. *Adv Opt Mater* **6**, 1701043 (2018).
 47. Xu K C, Wang Z Y, Tan C F, Kang N, Chen L W et al. Uniaxially stretched flexible surface plasmon resonance film for versatile surface enhanced Raman scattering diagnostics. *ACS Appl Mater Interfaces* **9**, 26341–26349 (2017).
 48. Zhao W J, Ghorannevis Z, Chu L Q, Toh M, Kloc C et al. Evolution of electronic structure in atomically thin sheets of WS₂ and WSe₂. *ACS Nano* **7**, 791–797 (2013).
 49. Lu G W, Zhang T Y, Li W Q, Hou L, Liu J et al. Single-molecule spontaneous emission in the vicinity of an individual gold nanorod. *J Phys Chem C* **115**, 15822–15828 (2011).
 50. Zhao J Y, Cheng Y Q, Shen H M, Hui Y Y, Wen T et al. Light emission from plasmonic nanostructures enhanced with fluorescent nanodiamonds. *Sci Rep* **8**, 3605 (2018).
 51. Anger P, Bharadwaj P, Novotny L. Enhancement and quenching of single-molecule fluorescence. *Phys Rev Lett* **96**, 113002 (2006).
 52. Zengin G, Wersäll M, Nilsson S, Antosiewicz T J, Käll M et al. Realizing strong light-matter interactions between single-nanoparticle plasmons and molecular excitons at ambient conditions. *Phys Rev Lett* **114**, 157401 (2015).

Acknowledgements

This work was supported by the National Key Research and Development Program of China (grant No. 2018YFB2200401) and the National Natural Science Foundation of China (grant Nos. 91950111, 61521004 and 11527901).

Author contributions

G. W. Lu supervised the project. S. Liu and A. Q. Hu prepared the samples. A. Q. Hu performed the experiments and wrote the manuscript. All authors contributed to the discussion of the data and the revision.

Competing interests

The authors declare no competing financial interests.

Supplementary information

Supplementary information for this paper is available at <https://doi.org/10.29026/oea.2019.190017>